Research Article

# Structural and photocatalytic properties of co-doped hybrid $ZrO_2$–$TiO_2$ photocatalysts

Nurshahnawal Yaacob[1,2,3] · Ahmad Fauzi Ismail[2,3] · Goh Pei Sean[2,3] · Noor Aina Mohd Nazri[4]



**Abstract**

In this study, pure $TiO_2$, $ZrO_2$, and hybrid $ZrO_2$–$TiO_2$ photocatalysts were synthesized through solgel process and calcined at three different temperatures. The synthesized photocatalysts were characterized using powder X-ray diffraction (PXRD), field-emission scanning electron microscopy (FESEM), Brunauer–Emmet–Teller (BET), ultraviolet–visible (UV–Vis) spectrometer, and photoluminescence (PL) spectrometer. The PXRD patterns show that the rutile phase of $TiO_2$ was suppressed through co-doping with $ZrO_2$ and produced small crystallite size. The hybrid photocatalysts with small crystallite size recorded the highest surface area of 114.7 $m^2/g$ compared to pure $TiO_2$ and $ZrO_2$ photocatalysts as confirmed by BET analysis. Irregular size and shape was observed in the hybrid photocatalysts compared to spherical shape and size in $TiO_2$ and flaky shape in $ZrO_2$ as shown by the FESEM images. The optical properties of the photocatalysts investigated using UV–Vis spectroscopy showed a decrease in band gap energy of pure $TiO_2$ through linear extrapolation from the Tauc's plot despite the slightly higher band gap energy of the hybrid photocatalysts. However, PL analysis showed that doping of $ZrO_2$ into $TiO_2$ increased the separation efficiency of the electron–hole pairs and enhanced the photocatalytic activity. The phenol degradation of the hybrid $ZrO_2$–$TiO_2$ photocatalysts was higher compared to those of the pure $TiO_2$ and $ZrO_2$.

**Keywords** Solgel · Hybrid $TiO_2$–$ZrO_2$ photocatalysts · Phenol degradation

## 1 Introduction

Traditional photocatalyst such as titanium dioxide or titania ($TiO_2$) [1] with metastable state structure of anatase has been broadly used for the photodegradation of organic pollutants in water and air owing to its low cost [2], environmental friendliness [3], excellent oxidative properties, long-term stability without secondary pollution [4, 5], quick oxidation, high photocatalytic activity, chemical stability, and titania nontoxicity [6]. Band gap energy around 3.2 eV for anatase $TiO_2$ makes this photocatalyst can only be activated under UV light irradiation despite attempts made to study photocatalytic activity of $TiO_2$ under irradiation of visible light. The anatase phase in $TiO_2$ was reported to transfer to the rutile phase and reduced the band gap to around 3.0 eV at calcination temperature above 650 °C. This offers many advantages such as absorbing small quantity of the solar spectrum, from transparent to incoming light [4]. Nevertheless, the intrinsic limitation of $TiO_2$ in terms of the recombination of the large amount of the photoactivated electrons and holes is still a main challenge to be addressed to further improve the quantum yield of the photocatalytic activity [7]. Among the advanced oxidation processes (AOP), heterogeneous photocatalysis is eminently used due to its environmentally friendly recognition and high oxidation efficiency [8–10].

Until now, the photocatalytic performance of $TiO_2$ is still widely investigated. The cytotoxicity assessment

✉ Ahmad Fauzi Ismail, afauzi@utm.my | [1]Malaysian Institute of Marine Engineering Technology (MIMET), Universiti Kuala Lumpur, 32200 Lumut, Perak, Malaysia. [2]Advanced Membrane Technology Research Centre (AMTEC), Universiti Teknologi Malaysia, 81300 Skudai, Johor, Malaysia. [3]Faculty of Chemical and Energy Engineering (FCEE), Universiti Teknologi Malaysia, 81300 Skudai, Johor, Malaysia. [4]Malaysian Institute of Chemical and Bio-Engineering Technology (MICET), Universiti Kuala Lumpur, 78000 Alor Gajah, Melaka, Malaysia.

SN Applied Sciences (2019) 1:252 | https://doi.org/10.1007/s42452-019-0247-4

Received: 11 November 2018 / Accepted: 11 February 2019 / Published online: 20 February 2019

using UV/$TiO_2$-based degradation system for anthraquinone Reactive Blue 19 (RB-19) showed less toxic nature of the transformed by-products of RB-19 [2]. Previously, the same researcher studied the $TiO_2$-assisted Reactive Black 5 (RB-5) degradation and disclosed that the toxicity of RB-5 reduced significantly after photocatalytic treatment [10]. The $TiO_2$/UV-assisted Rhodamine B degradation was reported to eliminate the toxicity of recalcitrant compounds and textile wastewater effluents [6] and later tested on Rhodamine 6G [9]. Urchin-like and yolk–shell $TiO_2$ microspheres synthesized using solgel for degradation of methylthionine chloride displayed better photocatalytic activity than that of the commercial P25 [3]. The optimization of old synthesis of $TiO_2$ nanoparticles to degrade methyl orange and bromothymol blue resulted in the best performance of $TiO_2$ nanoparticles of molar $C_{12}H_{28}O_4Ti$/$CO(NH_2)_2$ in a ratio of 2:1 at 50 °C [11]. Also, graphene–$TiO_2$ (GT) nanocomposites for photocatalytic degradation of methylene blue (MB) showed that GT-8wt% exhibited the best photocatalytic activity toward the photocatalytic degradation of MB [12]. Despite the improved photocatalytic activity reported, there are many other challenges such as controlling the particle size, homogeneity, and monodisperse ability of $TiO_2$ which can affect the surface area of $TiO_2$ and reduce the photocatalytic activity [3].

$TiO_2$ properties can be enhanced by adding another metal oxide [13]. The second metal oxide introduction, such as $ZrO_2$, $SiO_2$, $La_2O_3$, and $Fe_2O_3$, can generate new crystallographic stages with rather diverse properties than the original oxides and has proven to be a successful method to enhance the thermal stabilization of $TiO_2$ [4, 5, 13] and UV light photocatalytic activity [14, 15]. The particle size of $TiO_2$ can be reduced by adding a small quantity of $ZrO_2$ into $TiO_2$ owing to the different nuclei and coordination geometry. This has in turn increased the surface area of the photocatalyst [16] and acid–base properties [17]. However, the properties of photocatalyst particularly rely on the synthesis methods plus the way of processing. Thus, selecting the most proper technique for photocatalyst preparation is vital to achieve the desired chemical purity, phase, and morphology [18].

To improve the photocatalytic properties of $TiO_2$, a small quantity of $ZrO_2$ can be used for co-doping purpose. Even though $ZrO_2$ is considered as a poor photocatalyst due to its wide bad gap around 5 eV, doping of $ZrO_2$ into $TiO_2$ was reported to boost the photocatalytic practicality of advanced $ZrO_2$–$TiO_2$ mixed oxides [19]. $TiO_2$ doped by $ZrO_2$ was studied by many researchers [4, 7, 13, 14, 16–27] in the form of photocatalysts or thin film. These hybrid photocatalysts were prepared using various methods including solgel, polymer gel templating, homogeneous precipitation, and hydrothermal. Due to its higher photocatalytic activity compared to pure $TiO_2$ [21], the hybrid of $ZrO_2$ and $TiO_2$ has been widely investigated in the photocatalysis field by many researchers.

To the best of our knowledge, this paper is the first to study the nonporous or macroporous hybrid $ZrO_2$–$TiO_2$ photocatalysts for phenol degradation. Thus, this study attempts to produce hybrid $ZrO_2$–$TiO_2$ photocatalysts with enhanced photocatalytic activity. The influence of modified solgel method through sol evaporation at superheated temperature on the photocatalysts properties was analyzed using powder X-ray diffraction (PXRD), field-emission scanning electron microscopy (FESEM), Brunauer–Emmet–Teller (BET), ultraviolet–visible (UV–Vis) spectrometer, and photoluminescence (PL) spectrometer. The performance of the hybrid photocatalysts to enhance the photocatalytic activity was determined through phenol degradation and analyzed using high-performance liquid chromatography (HPLC).

## 2 Experimental procedures

### 2.1 Materials

Titanium(IV) isopropoxide (TTIP, 97%) and zirconium(IV) propoxide solution (TPZ, 70 wt% in 1-propanol) purchased from Sigma-Aldrich were used as the precursors for $TiO_2$ and $ZrO_2$. 2-Propanol anhydrous (99.5%), nitric acid (70%), and phenol (GR for analysis) were purchased from Sigma-Aldrich, RCI Labscan Limited, and Merck, respectively. All chemical reagents were used without further purification. Deionized (DI) water was used to prepare all photocatalysts as well as to dilute the phenol solution.

### 2.2 Synthesis of photocatalysts

$TiO_2$ photocatalysts were synthesized using solgel method as described earlier [8]. $TiO_2$ was prepared by mixing 10 mL of TTIP with 90 mL of IPA. The mixture was then added dropwise into 900 mL of DI water that was maintained at pH 1.5 using nitric acid by means of portable pH meter (HQ11d, HACH), and the mixture was mechanically stirred using a magnetic stirrer. The reaction tub temperature was kept approximately at 2 °C during the mixing process using crushed ice. The mixture was stirred vigorously for 20 h at ambient temperature which later formed a colloidal suspension known as sol. The sol was later aged for 24 h before being evaporated using a hot plate at a superheated temperature of 200 °C until the sol transformed into gel. The gel layer continued to evaporate to form $ZrO_2$–$TiO_2$ powder (photocatalysts). The photocatalysts obtained were dried at 105 °C for 4 h followed by calcination at 500, 600, and 700 °C in a furnace (Nabertherm GmbH) with air flowing continuously for 3 h. Calcination

at different temperatures was carried out to observe the stability of each photocatalyst especially on the effect of temperature on the transformation of $TiO_2$ anatase phase into rutile phase as studied earlier [4]. The dried photocatalysts were then ground into fine powder prior to testing. The hybrid $ZrO_2$–$TiO_2$ (1:1) photocatalysts were also prepared following the same experimental condition.

### 2.3 Characterization of photocatalysts

PXRD (D/max rB 12 kW, Rigaku @ D5000, Siemens) equipped with nickel-filtered copper Kα radiation ($\lambda$ = 1.54056 Å) operated at 30 mA and 40 kV was used to confirm the crystal structure of the photocatalysts. The measurement was executed by monitoring the diffraction angle $2\theta$ in the range of 5°–60° with a step increment of 0.05°. The photocatalysts powder was fitted into 20 × 20 × 0.5 mm sample holder for testing purpose.

Based on XRD data, the average crystallite sizes of the photocatalysts were estimated from the line broadening of (101) peak. The crystallite size, $B_{\text{crystallite}}$, was calculated using the Debye–Scherrer's equation [28] as shown by Eq. (1).

$$B_{\text{crystallite}}(\text{nm}) = \frac{K\lambda}{B_{hkl}\cos\theta} \tag{1}$$

where $K$ is the shape factor (0.94 for spherical crystallites with cubic symmetry), $B_{hkl}$ is the full width at half maximum (fwhm) of the peak in radian corrected for instrumental broadening, $\lambda$ is the radiation wavelength, and $\theta$ is the Bragg angle (half of the incident angle of $2\theta$ in radian).

The micrographs of the photocatalysts were obtained using Zeiss FESEM Crossbeam 340 instrument to investigate the surface morphology of the photocatalysts. The powder samples were spread evenly over carbon tape used as substrate and coated with a thin layer of gold prior to analysis. The surface area, pore volume, and pore size of the photocatalysts were determined using Thermo Scientific surface analyzer. The BET method was used to obtain the surface area and pore volume. Meanwhile, Barrett–Joyner–Halenda (BJH) model was used to determine the pore size of the photocatalysts derived from the adsorption branch of the isotherm. The measurement was performed by the $N_2$ adsorption isotherm at 77 K. Prior to analysis, the samples were degassed at 200 °C for 2 h.

Perkin Elmer LAMBDA™ 1050 UV–Vis–NIR spectrometer was used to record the reflectance spectra measured in the 325–500 nm range for optical band gap estimation and investigate the impact of coupling $ZrO_2$ metal oxide on the band gap of $TiO_2$. The band gap energy of the photocatalysts was estimated based on reflectance spectra using Kubelka–Munk theory which combines the raw reflectance data R with the absorption coefficient $\alpha$ [29] as shown in Eq. (2):

$$F(R) = \frac{\alpha}{s} = \frac{(1-R)^2}{2R} \tag{2}$$

The scattering factor, s, in Eq. (2) is wavelength independent. Thus, the Kubelka–Munk function $F(R)$ is proportional to α for highly light-scattering materials and absorbing particles in a matrix [30] as shown in Eq. (3):

$$F(R) \approx \alpha \tag{3}$$

In this study, the modified Kubelka–Munk function was used as shown in Eq. (4) through multiplication of F(R) with $h\nu$ using the corresponding coefficient n associated with an electronic transition:

$$(F(R)\cdot h\nu)^n \tag{4}$$

The optical band gap energy $E_g$ was obtained from the $(F(R)\cdot h\nu)^n$ versus $h\nu$ plot which is also known as Tauc's plot. The values of $n = 2$ for direct allowed transition and $n = 1/2$ for an indirect allowed transition were employed in this study for comparison purpose. The fluorescence emission spectrum of the photocatalysts was obtained using Perkin Elmer LS55 fluorescence spectrometer. The phenol concentration and the intermediate compounds produced during its degradation were quantitatively analyzed using HPLC system (Agilent Technologies 1220 Infinity LC).

### 2.4 Photocatalytic activity evaluation

Photocatalytic activities of the prepared photocatalysts were measured via the degradation of phenol in aqueous solution under UV light irradiation at atmospheric pressure and room temperature. About 0.35 g of photocatalysts was initially dispersed into 350 mL of phenol solution at a starting concentration of 10 ppm and later at 40 ppm at around pH 6 under magnetic stirring to ensure uniform conditions of the reacting mixture. Prior to photocatalytic testing, the prepared suspension was stirred at 298 K in the dark for 120 min to establish the adsorption–desorption equilibrium of phenol on the photocatalyst. The photooxidation of phenol was carried out through a cylindrical quartz photoreactor, and the illumination distance was fixed at 1 cm from the reacting mixture. The suspension was then irradiated using an 8 W black light blue UV-A lamp with a maximum light intensity output at 365 nm (FL8BLB, Sankyo Denki Co., Ltd., Japan). The UV light intensity was measured using a UVX radiometer (UVP Inc., Upland, CA) with UV-A sensor (UVX-36, UVP Inc., Upland, CA). Samples were collected from the suspension in consistent intervals (3 mL of aliquot was withdrawn from the suspensions every 30 min within 4 h of irradiation) to evaluate the apparent reaction rate constant, and the photocatalyst

was filtered through 0.2 µm PTFE membrane before analyzing it using HPLC–UV at 254 nm. The phenol degradation in aqueous solution was determined using Eq. (5).

$$\text{Degradation}(\%) = \frac{C_0 - C_t}{C_0} \times 100\% \quad (5)$$

where $C_0$ is the initial concentration at time $t = 0$, and $C_t$ is the concentration at time interval.

## 3 Results and discussion

### 3.1 Effect on crystal structure

The XRD patterns of pure $TiO_2$, $ZrO_2$, and hybrid $ZrO_2$–$TiO_2$ photocatalysts calcined at 500 °C are shown in Fig. 1a. The sharp and narrow peaks confirmed that the photocatalysts are of high quality with good crystallinity and fine grain size. Pure $TiO_2$ exhibited mixed diffraction peaks with anatase phase at $2\theta = 25.3°$ (101), 37.8° (004), 48.0° (200), 53.8° (105), and 55.0° (211) as indexed in ICDD DB card no. 01-089-4203 together with 27.4° (110), 36.0° (101), 41.2° (111), 55.0° (211), and 56.6° (220) which are the characteristics peaks with rutile phase as indexed in ICDD DB card no. 01-078-4189 through qualitative measurement. An intense anatase peak was observed at peak (101) with 80 wt% of reference intensity ratio (RIR) value for anatase phase. Diffraction peaks of pure $ZrO_2$ which appeared at $2\theta = 24.1°$ (011), 28.1° (– 111), 31.4° (111), 34.2° (002), and 50.1° (220) indicate the characteristic peaks with baddeleyite phase as indexed in ICDD DB card no. 01-083-0940 together with the characteristics peaks with tetragonal phase at $2\theta = 30.2°$ (101), 35.1° (110), 50.1° (112), 54.0° (200), and 60.0° (211) as indexed in ICDD DB card no. 01-080-0965. The hybrid $ZrO_2$–$TiO_2$ presented mixed characteristic diffraction peaks of anatase $TiO_2$ at (101), (200), (105), (211), and (204) as indexed in ICDD DB card no. 01-071-1169, and as well as, pure tetragonal phase of $ZrO_2$ at (101), (110), (200), (112), and (211) as indexed in ICDD DB card no. 01-080-0965 indicates that $ZrO_2$ affected the crystallinity of $TiO_2$ which contradict the findings reported elsewhere [31]. The baddeleyite phase was suppressed, leaving only the desired tetragonal phase with all matching peaks. However, the $TiO_2$ patterns were observed to be more intense because $TiO_2$ diffracts more efficiently compared to $ZrO_2$ with at least four peaks matching the principal diffraction peaks of pure $TiO_2$ with a small amount of mismatch in peak position. These results were supported by the RIR values that showed anatase phase contents of 45.2 wt%.

For photocatalysts calcined at 600 °C as shown in Fig. 1b, pure $TiO_2$ showed mixed anatase–rutile phase with anatase dominated. However, slightly significant

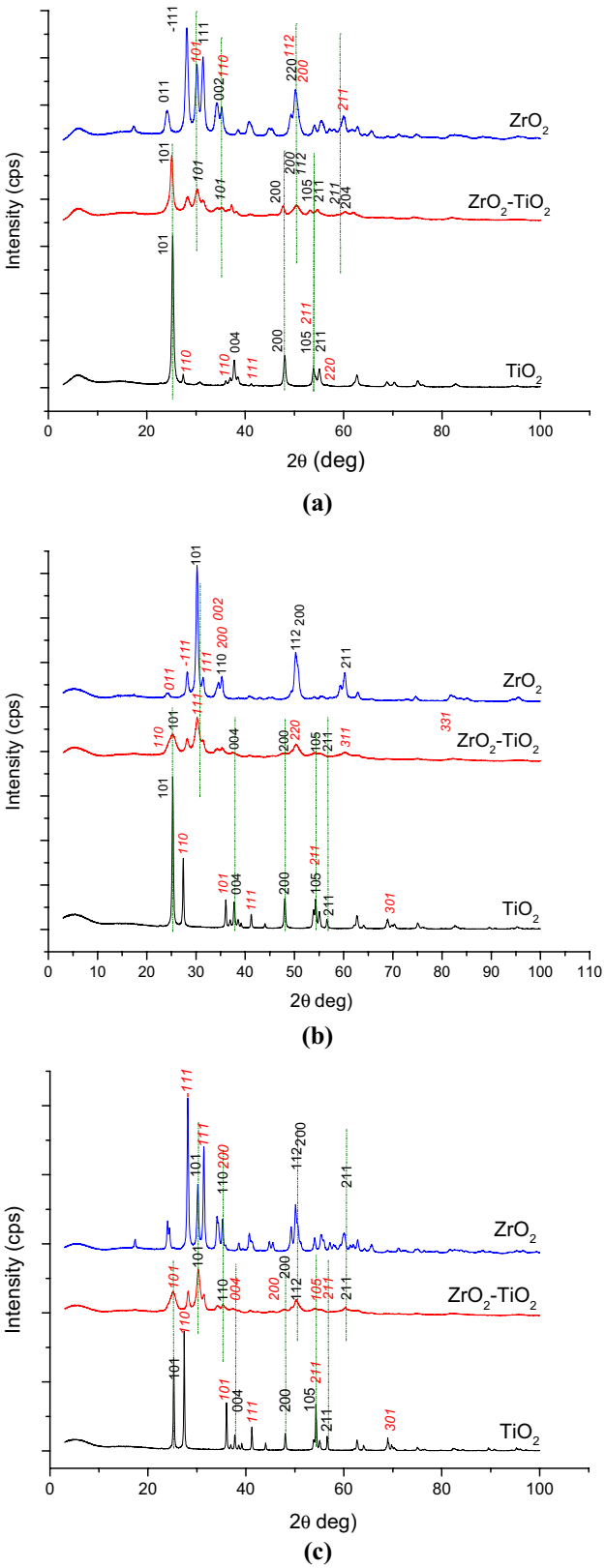


**Fig. 1** XRD patterns of pure $TiO_2$, $ZrO_2$, and hybrid $ZrO_2$–$TiO_2$ photocatalysts calcined at **a** 500 °C, **b** 600 °C, and **c** 700 °C

rutile peaks emerged when the calcination temperature was increased. The hybrid $ZrO_2$–$TiO_2$ presented a mixed zirconia–anatase phase with diffraction peaks of $ZrO_2$ and $TiO_2$ indexed in ICCD DB card no. 01-079-1796 and 01-075-2553, respectively, with dominant orthorhombic zirconia phase surpassed over anatase phase. No rutile phase was observed. This shows that the addition of $ZrO_2$ stabilized the anatase titania phase [17]. Pure $ZrO_2$ showed mixed diffraction peaks of tetragonal–monoclinic phase with ICCD DB card no. 01-079-1765 and 01-078-0047, respectively. The tetragonal phase showed an intense peak at peak (101) compared to the monoclinic phase although the RIR values showed that 95 wt% of the content was dominated by monoclinic phase. The hybrid $ZrO_2$–$TiO_2$ displayed a mixed orthorhombic–anatase phase with ICCD DB card no. 01-079-1796 and 01-075-2553, respectively. An intense orthorhombic peak was observed at peak $2\theta = (111)$.

When calcined at 700 °C, as shown in Fig. 1c, $TiO_2$ exhibited a mixed rutile–anatase phase with intensity of rutile peaks observed throughout the XRD pattern indicating the transfer of anatase phase to rutile phase at temperature above 650 °C [4]. A highly intense peak (110) of rutile phase was observed compared to peak (101) of anatase phase. The results obtained are in line with the RIR values which recorded that 59.8 wt% of the content is in rutile phase. Pure $ZrO_2$ exhibited a mixed baddeleyite–tazheranite phase as indexed in ICCD DB card no. 01-075-9454 and 01-072-7115, respectively, with intensity in the baddeleyite peak observed at peak (− 111). The baddeleyite phase recorded 81.2 wt% of the RIR value. The hybrid $ZrO_2$–$TiO_2$ showed a zirconia-rich composition with intense $ZrO_2$ diffraction peaks in zirconia (nanocrystalline) at peak (101) indexed in ICCD DB card no. 01-070-6627 and strong peak (− 111) of monoclinic phase indexed in ICCD DB card no. 01-078-0047, together with $TiO_2$ in anatase phase indexed in ICCD DB card no. 01-071-1168. The RIR values recorded that 40.4 wt% of the contents is in the zirconia (nanocrystalline) phase.

As observed earlier, the photocatalysts calcined at 500 °C showed the best characteristics and was further investigated due to the presence of only a small rutile phase in pure $TiO_2$ photocatalysts, no rutile phase in the hybrid photocatalysts, and the presence of a mixed monoclinic–tetragonal phase in pure $ZrO_2$ photocatalysts. From the results, the crystallite size of $TiO_2$ was 20.07 nm. $ZrO_2$ doping successfully reduced the crystallite size of hybrid $ZrO_2$–$TiO_2$ to 14.29 nm which was much smaller compared to 72 nm as reported elsewhere [22] at the same photocatalysts molarity. This indicates that $ZrO_2$ doping had an impact on $TiO_2$ by suppressing the anatase crystallite growth which in turn reduced the crystallite size of $TiO_2$ and contributed to a larger surface area. Table 1 summarizes crystallite size for all photocatalysts.

Figure 2 shows the FESEM images of the pure $TiO_2$, $ZrO_2$, and hybrid $ZrO_2$–$TiO_2$ photocatalysts calcined at 500 °C. It was observed that the shape of pure $TiO_2$ photocatalysts was nearly spherical and cubical with a particle size of around 63 nm. The aggregation of $TiO_2$ photocatalysts was due to strong interaction between crystallites. Pure $ZrO_2$ exhibited irregular flaky shapes. The particle size recorded for pure $ZrO_2$ was in the range of 33–41 nm. The hybrid $ZrO_2$–$TiO_2$ photocatalysts with 50% of $ZrO_2$ revealed a smaller and uniform spherical shape with a particle size in the range of 24–53 nm compared to that of $TiO_2$. This shows that co-doping $ZrO_2$ into $TiO_2$ could control both the particle size of $TiO_2$ and the shape of the particles [7] to produce uniformly dispersed aggregates.

Figure 3 shows the $N_2$ adsorption–desorption hysteresis loops of the nanoporous photocatalysts observed for a wide range of relative pressure $P/P_0$. The isotherms obtained for all photocatalysts demonstrated Type II isotherm with an H4 hysteresis loop which indicates nonporous or macroporous nature of the materials. However, the extensive photocatalytic application of the photocatalysts was attributed by the nanosized particles, high surface area, and optimum pore volume [32]. The hybrid $ZrO_2$–$TiO_2$ photocatalysts demonstrated significant increase in surface area with 114.7 $m^2/g$ as a result of co-doping of $ZrO_2$ into $TiO_2$ compared to pure $TiO_2$ and $ZrO_2$ with the surface areas of 39.9 and 48.8 $m^2/g$, respectively. Similar results were reported indicating the effective role of $ZrO_2$ to suppress the growth of $TiO_2$ crystals [22, 28]. The hybrid $ZrO_2$–$TiO_2$ photocatalysts also recorded the highest pore volume at 0.31 $cm^3/g$, followed by $ZrO_2$ at 0.22 $cm^3/g$ and $TiO_2$ at 0.13 $cm^3/g$. The pore size of the hybrid photocatalysts increased more than that of the pure $TiO_2$, but less than that of the pure $ZrO_2$. Table 2 summarizes the properties from BET analysis. Higher surface area and pore volumes were associated with the increase in surface active sites and channels. These properties allow various organic pollutants to diffuse rapidly during photocatalytic activity which in turn increases the photodegradation reaction rate [33, 34].

**Table 1** Crystallite size of photocatalysts (based on most intense peak) calcined at 500–700 °C

| Photocatalysts | Crystallite size (nm) | | |
|---|---|---|---|
| | 500 °C | 600 °C | 700 °C |
| $TiO_2$ | 20.1 | 29.9 | 51.5 |
| $ZrO_2$ | 13.7 | 18.3 | 28.0 |
| $ZrO_2$–$TiO_2$ | 14.3 | 11.1 | 11.4 |

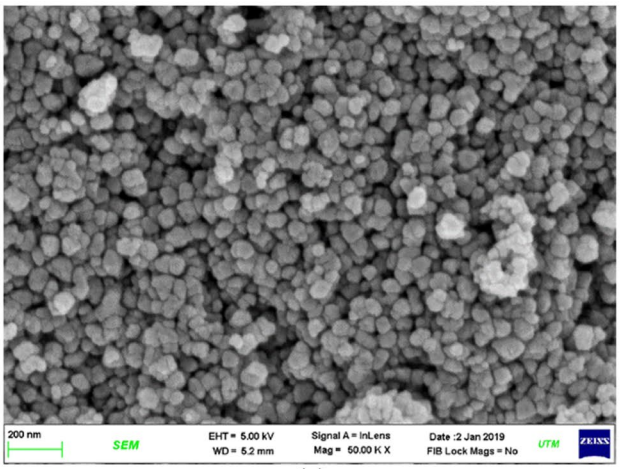


(a)

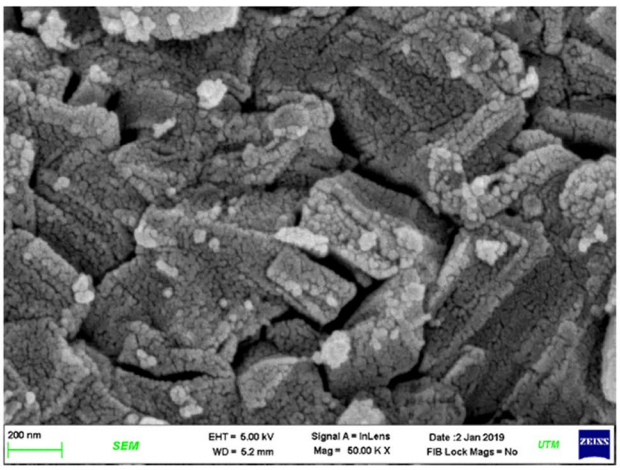


(b)

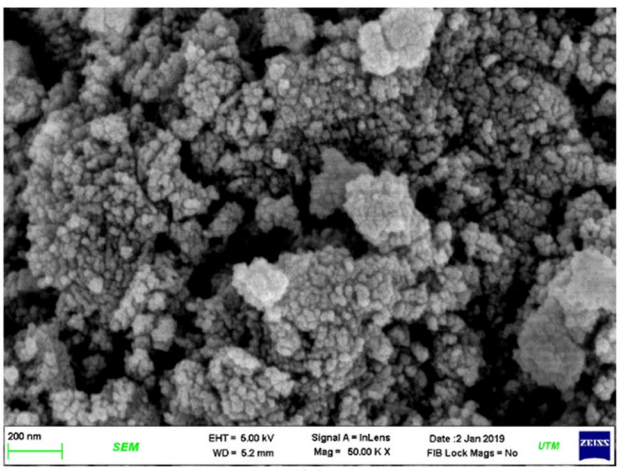


(c)

**Fig. 2** FESEM images of **a** pure $TiO_2$, **b** $ZrO_2$, and **c** hybrid $ZrO_2$–$TiO_2$ photocatalysts calcined at 500 °C for 3 h with magnification of ×50 000

### 3.2 Effect on optical band gap

Figure 4 shows the spectral reflectance curves of pure $TiO_2$ and hybrid $ZrO_2$–$TiO_2$ calcined at 500–700 °C. A smooth curve increment was observed when calcined at 500 and 600 °C. However, at 700 °C, irregular curve pattern was observed from the early stage of radiation despite the smooth curve throughout the UV region. This was probably contributed by the increase in crystallite size as shown in Table 1 or structural changes with increasing calcination temperature. Thus, only the optical band at 500 and 600 °C was further measured. The photocatalysts with the best optical band gap were used to evaluate the photocatalytic activity for phenol degradation.

The $E_g$ values of $TiO_2$ and hybrid $ZrO_2$–$TiO_2$ obtained through direct extrapolation of the Kubelka–Munk function as shown in Fig. 5 for calcination at 500 °C were 3.07 and 3.34 eV for indirect allowed transition, respectively. For direct allowed transition, the $E_g$ values were 3.09 and 3.35 eV, respectively. At 600 °C, the $E_g$ values of $TiO_2$ were 3.16 and 3.14 eV for indirect and direct allowed transition, respectively, as shown in Fig. 6. The presence of a small rutile phase was responsible in giving the $E_g$ value of $TiO_2$ of 3.0 eV. However, as the rutile phase was suppressed, the $E_g$ of the hybrid photocatalyst increased to the widely reported $E_g$ values of $TiO_2$ around 3.2 eV [4, 5]. The $E_g$ values for hybrid $ZrO_2$–$TiO_2$ were higher at 3.36 and 3.37 eV, respectively. The $E_g$ values for $TiO_2$ reported in this study for both transitions were much lower compared to the $E_g$ values reported elsewhere [30] at 3.30 and 3.72 eV, respectively. Both transitions were suitable to be used for $E_g$ estimation due to the small differences.

The small changes in the $E_g$ values of the hybrid $ZrO_2$–$TiO_2$ compared to that of pure $TiO_2$ for both transitions at different calcination temperatures suggest that the thermal stability of $TiO_2$ improved through $ZrO_2$ doping. Based on the $E_g$ values, both photocatalysts calcined at 500 °C showed better results. Therefore, the present work was further tested for oxidative photodegradation of phenol. The doping of $ZrO_2$ into $TiO_2$ could increase the separation efficiency of the electron–hole pairs and enhance the photocatalytic activity. The fluorescence intensity with higher value from the PL spectra indicates more recombination of electron–hole pairs which leads to lower photocatalytic activity [35].

The PL spectra of $TiO_2$, $ZrO_2$, and hybrid $ZrO_2$–$TiO_2$ calcined at 500 °C with excitations at 4.00, 4.78, and 4.14 eV presented in Fig. 7 exhibited a broad emission in the spectral range from 2.3–3.5 eV, 2.5–3.7 eV, and 2.3–3.6 eV for all respective three photocatalysts. The presence of peaks/shoulders at 2.96/2.60 eV for $TiO_2$, 2.97 and 3.13/2.83 eV for $ZrO_2$, and 3.19/2.98 eV for $TiO_2$–$ZrO_2$ was recorded. The hybrid $ZrO_2$–$TiO_2$ photocatalysts showed the lowest

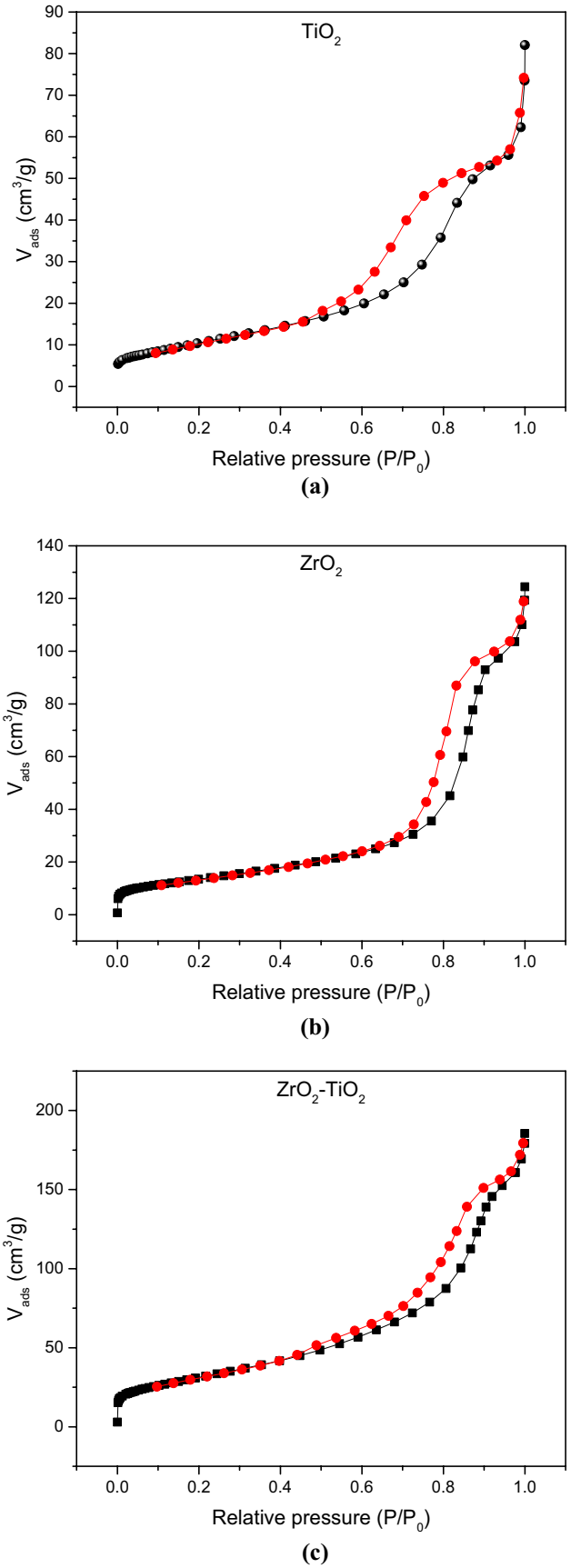


**Fig. 3** $N_2$ adsorption–desorption isotherm of **a** $TiO_2$, **b** $ZrO_2$, and **c** ▸ hybrid $ZrO_2$–$TiO_2$ with inset is BJH pore size distribution from desorption branch of isotherm

fluorescence intensity value compared to the pure $TiO_2$ and $ZrO_2$ photocatalysts which indicates that the electron–hole pairs recombination had been successfully suppressed and increased the photocatalytic activity. Even though doping of $ZrO_2$ into the $TiO_2$ lattice resulted in a slightly higher band gap, the electron lifetime on the conduction band can be prolonged [25] due to the increase in interfacial charge transfer that participates in the degradation reactions. This has consequently improved the photocatalytic activity [4, 36].

### 3.3 Effect on photocatalytic activity

The photocatalytic activity of pure $TiO_2$, hybrid $ZrO_2$–$TiO_2$, and pure $ZrO_2$ photocatalysts was tested for both adsorption (dark experiment) and oxidative photodegradation (experiment under illumination) of phenol at 10 and 40 ppm. The experiment with hybrid $ZrO_2$–$TiO_2$ in the dark showed that approximately 26% of the phenol at 10 ppm on the photocatalysts surface was adsorbed in 2 h. Interestingly, $ZrO_2$ showed somewhat active activity in the early of adsorption stage with 20% phenol adsorbed and followed by $TiO_2$ at 11% as shown in Fig. 8. The small crystallite size and high surface area of the photocatalysts were believed to contribute to the significant adsorption of phenol especially at 10 ppm. On the other hand, both hybrid $ZrO_2$–$TiO_2$ and $ZrO_2$ photocatalysts showed a much lower phenol adsorption of around 15% each at 40 ppm and only 11% of phenol adsorbed by $TiO_2$.

The photocatalytic experiment was evaluated after the adsorption–desorption equilibrium period. However, the phenol degradation was not completely elucidated because of the increase in peaks area from HPLC analysis due to the formation and transformation of intermediates [37]. The process of phenol degradation was visualized from HPLC chromatogram which acted as an indicator for the presence of chemicals with various intermediate compounds as shown in Figs. 9, 10 and 11 with the maximum peak height for phenol at a retention time of about 3.03 min. The retention times for the intermediate compounds were shorter compared to that of the parent phenol compound. During the adsorption–desorption stage of 120 min, at least four intermediate compounds were detected at the retention times of 1.9, 2.1, 3.3, and 3.5 min. Only two intermediate compounds were detected at the end stage of phenol degradation of 360 min at the retention times of 1.8 and 3.3 min. The intermediate compounds might be due to the formation of compounds such as hydroquinone, *p*-benzoquinone, and catechol [22, 38]

**Table 2** BET properties

| Photocatalysts | Surface area ($m^2$/g) | Pore volume ($cm^3$/g) | Pore radius (nm) |
|---|---|---|---|
| $TiO_2$ | 39.9 | 0.13 | 3.68 |
| $ZrO_2$ | 48.8 | 0.22 | 5.27 |
| $ZrO_2$–$TiO_2$ | 114.7 | 0.31 | 4.95 |

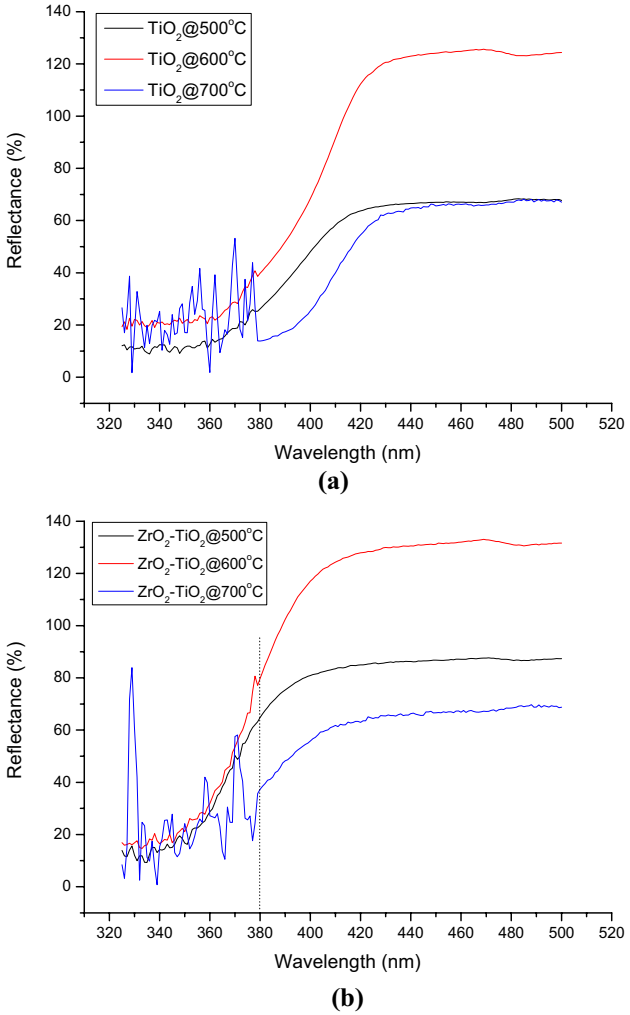


**Fig. 4** Diffuse reflectance spectra at different calcination temperatures for **a** pure $TiO_2$, and **b** hybrid $ZrO_2$–$TiO_2$ photocatalysts

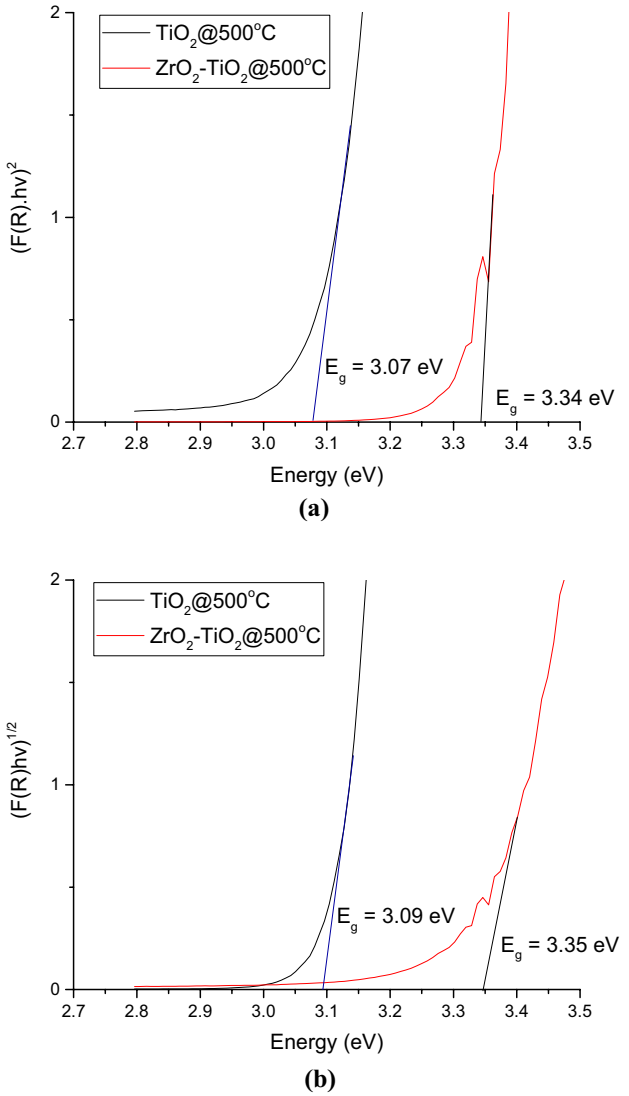


**Fig. 5** Optical band gap of $TiO_2$ and hybrid $ZrO_2$–$TiO_2$ photocatalysts at calcination temperature of 500°C for different transitions **a** indirect allowed **b** direct allowed

which can be confirmed through GC analysis. The peak intensity corresponding to phenol also showed decreasing trends within the 4 h degradation under UV light irradiation with a profound effect observed in the hybrid $ZrO_2$–$TiO_2$ photocatalysts. The degradation ability of the hybrid photocatalysts improved with $ZrO_2$ co-doping into the $TiO_2$ lattice. To guarantee the establishment of the adsorption–desorption equilibrium [39] despite normal adsorption–desorption stage of 30 min [7, 31] to 60 min [22], 120 min of adsorption–desorption stage was chosen.

Careful observation on phenol degradation by pure $ZrO_2$ showed that $ZrO_2$ can also act as a photocatalysts following the reduction of the intermediate compounds. The same result was observed elsewhere for phenol degradation at 25 ppm [22]. This was probably due to the lower $E_g$ values of the prepared $ZrO_2$ at around 3.15–3.17 eV. $ZrO_2$ was reported to have the $E_g$ values between 3.25 and 5.1 eV, depending on the sample preparation technique [40]. The observed photodegradation activity for phenol follows this order: hybrid $ZrO_2$–$TiO_2$ photocatalysts > pure $TiO_2$ photocatalysts > pure $ZrO_2$ photocatalysts. The increased photocatalytic activity was probably due to the presence of more hydroxyl groups

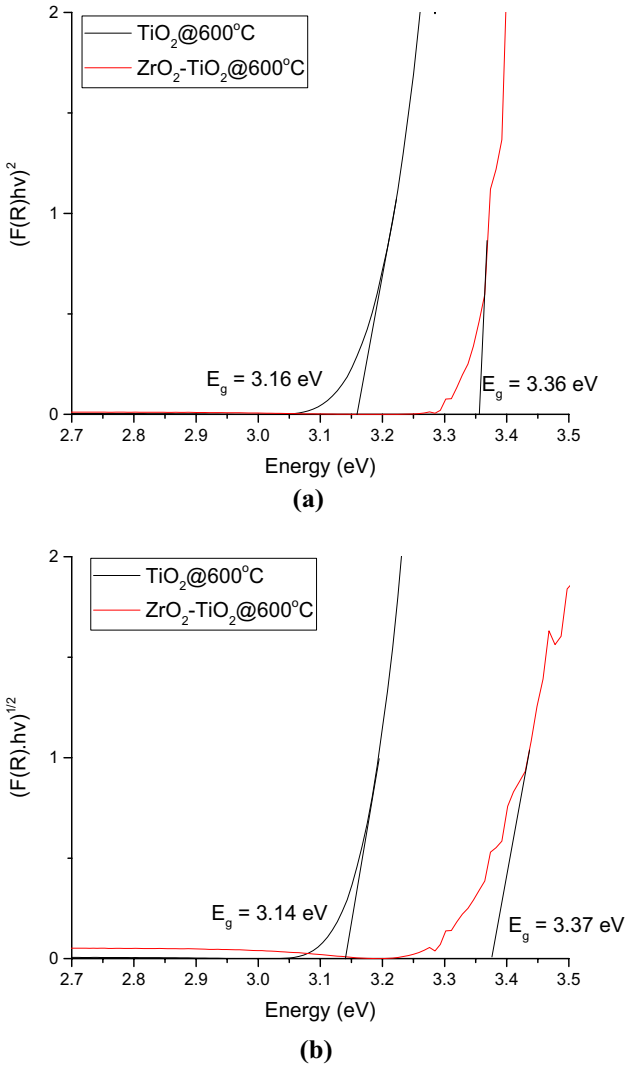


**Fig. 6** Optical band gap of $TiO_2$ and hybrid $ZrO_2$–$TiO_2$ photocatalysts at calcination temperature of 600°C for different transitions **a** indirect allowed **b** direct allowed

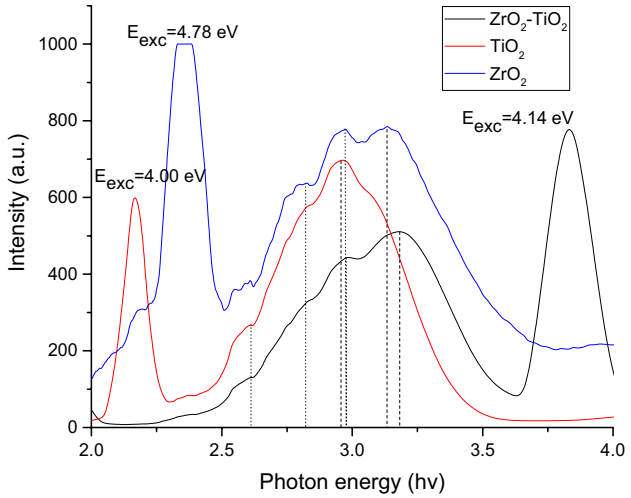


**Fig. 7** PL spectrum of $TiO_2$, $ZrO_2$, and $ZrO_2$–$TiO_2$ photocatalysts at 500°C

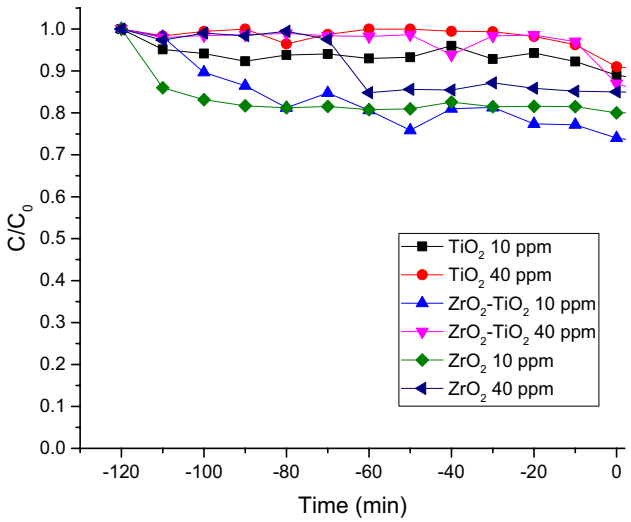


**Fig. 8** Adsorption activity of phenol

on the photocatalysts surface that inhibited the recombination of electron–hole pairs by trapping holes and generated powerful oxidants such as OH· radicals [7, 22].

Similarly, the separation of electron and hole between $TiO_2$ and $ZrO_2$ in the hybrid photocatalysts may also take place due to the energy level in both valence band (VB) and conduction band (CB) of the pure $TiO_2$ that corresponds well within the band gap of pure $ZrO_2$. During the excitation of electrons from the hybrid photocatalysts, most electrons from the CB of $ZrO_2$ easily transfer to the CB of $TiO_2$ from thermodynamic considerations, which inhibits the electron–hole pairs recombination [16]. The results did not represent total degradation, but serve as an indicator of potentially effective photocatalysts.

## 4 Conclusion

In this work, hybrid $ZrO_2$–$TiO_2$ photocatalysts synthesized using solgel method showed higher phenol degradation than those of the pure $TiO_2$ and $ZrO_2$ after being exposed to UV light. This is due to the small crystallite size and higher surface area exhibited by the hybrid $ZrO_2$–$TiO_2$ photocatalysts. The shape and size of the hybrid $ZrO_2$–$TiO_2$ photocatalysts also impacted the photocatalytic activity. The reduction of intermediate compounds at the end of the degradation process indicates

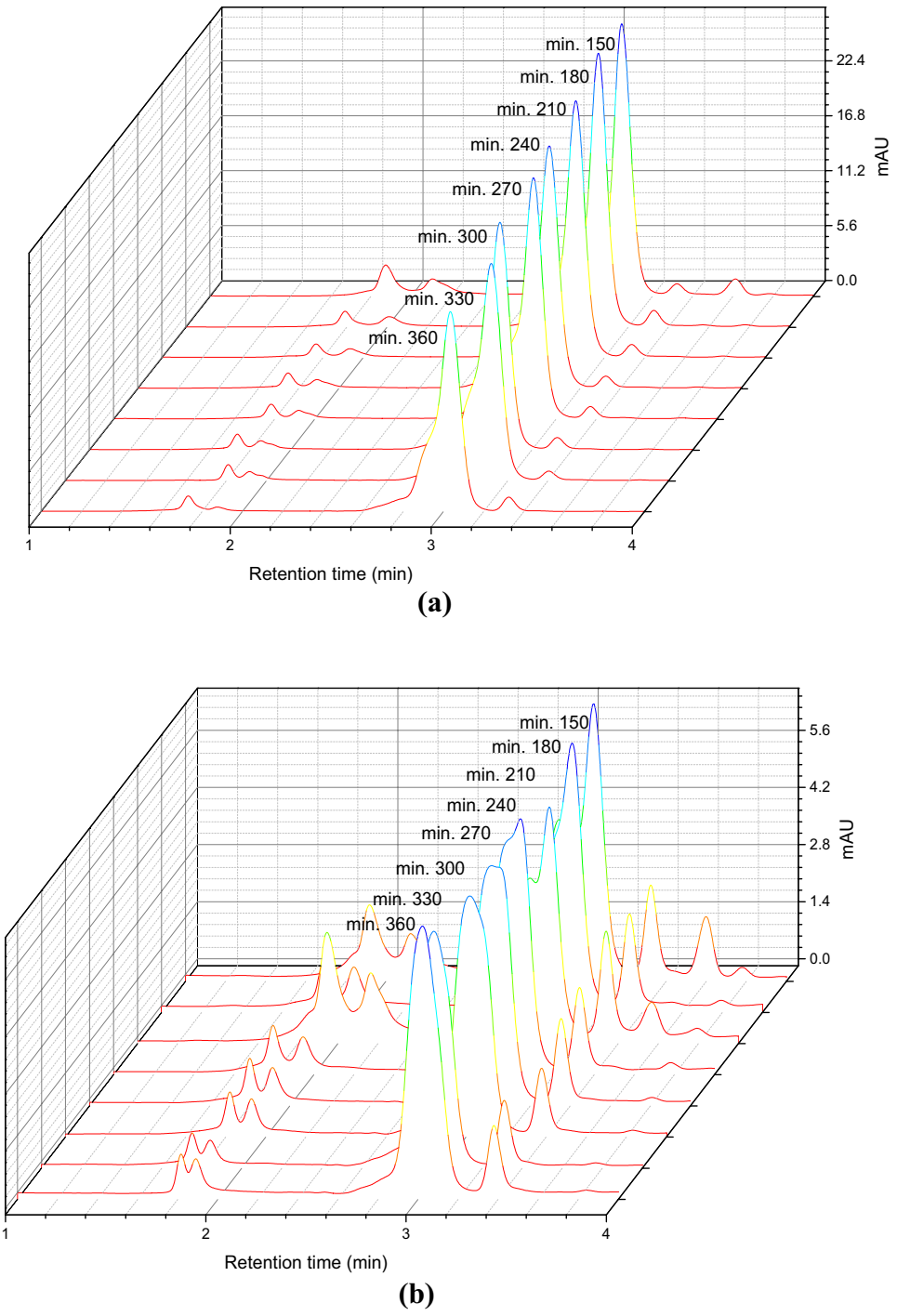


**Fig. 9** Chromatograms of $TiO_2$ photocatalysts at different running times under UV light for phenol photodegradation at **a** 10 ppm and **b** 40 ppm

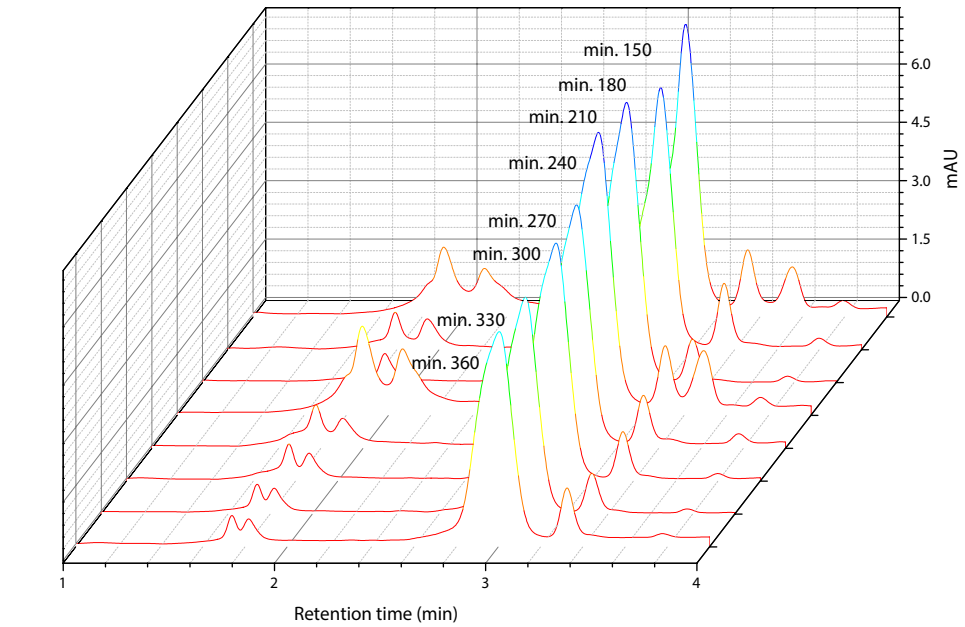


**(a)**

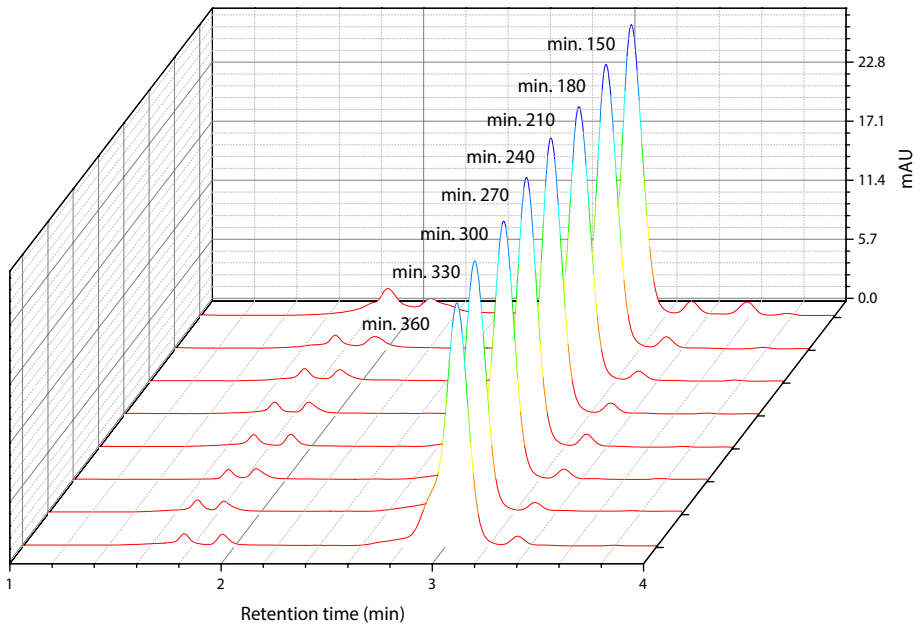


**(b)**

**Fig. 10** Chromatograms of $ZrO_2$–$TiO_2$ photocatalysts at different running times under UV light for phenol photodegradation at **a** 10 ppm and **b** 40 ppm

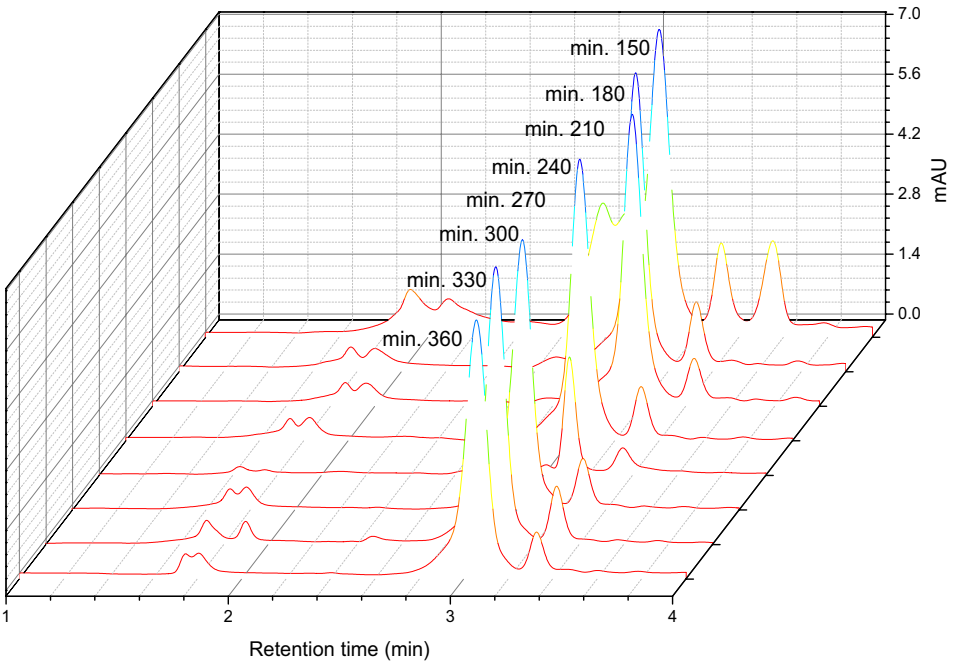


**(a)**

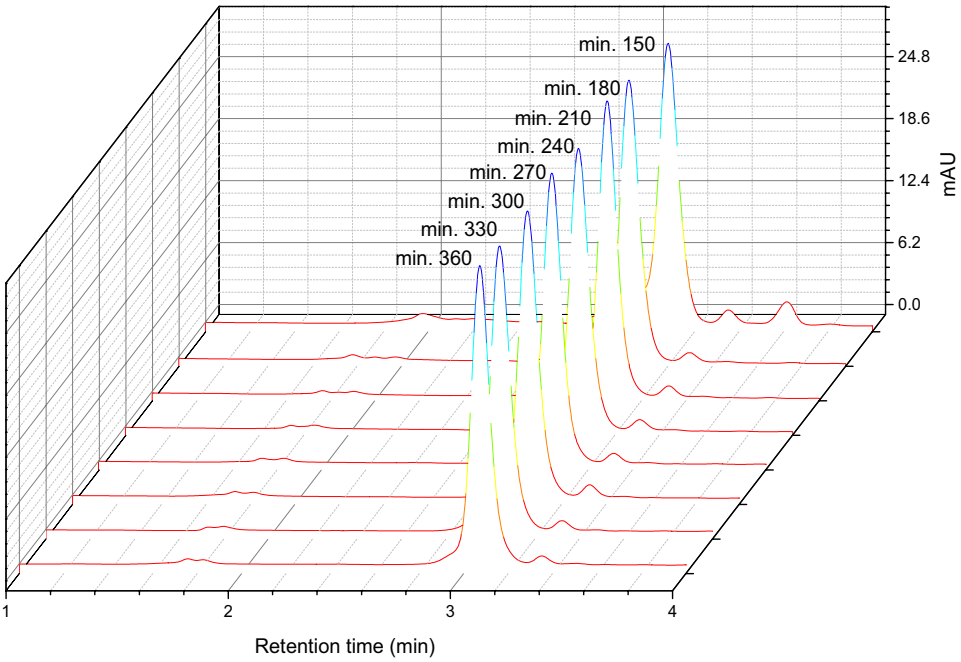


**(b)**

**Fig. 11** Chromatograms of $ZrO_2$ photocatalysts at different running times under UV light for phenol photodegradation at **a** 10 ppm and **b** 40 ppm

the hybrid $ZrO_2$–$TiO_2$ photocatalysts potential to remove phenol in wastewater. In general, co-doping of $ZrO_2$ into the $TiO_2$ lattice could address the low photocatalytic activity of a single metal oxide photocatalyst such as $TiO_2$ and suppressed the electron–hole pairs recombination to improve the photocatalysts performance.

**Funding** This work was financially supported by the Universiti Teknologi Malaysia (Project No. R.J090301.7809.4J195) under the Research University Grant and Ministry of Higher Education Malaysia.

## Compliance with ethical standards

**Conflict of interest** On behalf of all authors, the corresponding author states that there is no conflict of interest.

## References

1. Zhang C, Han P, Lu X, Mao Q, Qu J, Li Y (2018) Preparation and photocatalytic activity characterization of activated carbon fiber–$BiVO_4$ composites. RSC Adv 8:24665
2. Bilal M, Rasheed T, Iqbal HMN, Li C, Wang H, Hu H, Wang W, Zhang X (2018) Photocatalytic degradation, toxicological assessment and degradation pathway of C.I. Reactive Blue 19 dye. Chem Eng Res Des 129:384–390
3. Guo Z, Wang Q, Shen T, Kuang J, Cao W (2018) Synthesis of Urchin-like and Yolk–shell $TiO_2$ microspheres with enhanced photocatalytic properties. Environ Technol 7:1–25
4. Kim JY, Kim CS, Chang HK, Kim TO (2010) Effects of $ZrO_2$ addition on phase stability and photocatalytic activity of $ZrO_2$/$TiO_2$ nanoparticles. Adv Powder Technol 21:141–144
5. Tomar LJ, Chakrabarty BS (2013) Synthesis, structural and optical properties of $TiO_2$–$ZrO_2$ nanocomposite by hydrothermal method. Adv Mater Lett 4(1):64–67
6. Rasheed T, Bilal M, Iqbal HMN, Shah SZH, Hu H, Zhang X, Zho Y (2017) $TiO_2$/UV-assisted Rhodamine B degradation: putative pathway and identification of intermediates by UPLC/MS. Environ Technol 39(12):1533–1543
7. Neppolian B, Wang Q, Yamashita H, Choi H (2007) Synthesis and characterization of $ZrO_2$–$TiO_2$ binary oxide semiconductor nanoparticles: application and interparticle electron transfer process. Appl Catal A 333:264–271
8. Yao T, Jia W, Feng Y, Zhang J, Lian Y, Wu J, Zhang X (2018) Preparation of reduced graphene oxide nanosheet/FexOy/nitrogen-doped carbon layer aerogel as photo-Fenton catalyst with enhanced degradation activity and reusability. J Hazard Mater 362:62–71
9. Rasheed T, Bilal M, Iqbal HMN, Hu H, Zhang X (2017) Reaction mechanism and degradation pathway of rhodamine 6G by photocatalytic treatment. Water Air Soil Pollut 228(8):291
10. Bilal M, Rasheed T, Iqbal HMN, Hu H, Wang W, Zhang X (2018) Toxicological assessment and UV/$TiO_2$-based induced degradation profile of reactive black 5 dye. Environ Manage 61(1):171–180
11. Lusvardi G, Barani C, Giubertoni F, Paganelli G (2017) Synthesis and characterization of $TiO_2$ nanoparticles for the reduction of water pollutants. Materials 10:1208
12. Divya KS, Madhu AK, Umadevi TU, Suprabha T, Nair PR, Mathew S (2017) Improving the photocatalytic performance of $TiO_2$ via hybridizing with graphene. J Semicond 38(6):063002
13. Bensaha R, Bensouyad H (2012) Synthesis, characterization and properties of zirconium oxide ($ZrO_2$)-doped titanium ($TiO_2$) thin films obtained via sol-gel process. In: Heat treatment-conventional and applications. InTech, pp 207–234
14. Tian G, Pan K, Honggang F, Liqiang J, Zhou W (2009) Enhanced photocatalytic activity of S-doped $TiO_2$-$ZrO_2$ nanoparticles under visible-light Irradiation. J Hazard Mater 166:939–944
15. Kim JY, Kim CS, Chang HK, Kim TO (2011) Synthesis and characterization of N-doped $TiO_2$/$ZrO_2$ visible light photocatalysts. Adv Powder Technol 22:443–448
16. Fu X, Clark LA, Yang Q, Anderson MA (1996) Enhanced photocatalytic performance of titania-based binary metal oxide: $TiO_2$/$SiO_2$ and $TiO_2$/$ZrO_2$. Environ Sci Technol 30:647–653
17. Kan C, Liu X, Duan G, Wang X, Yang X, Lu L (2007) Synthesis and characterization of the air-water interfacial $TiO_2$/$ZrO_2$ binary oxide film. J Colloid Interface Sci 310:643–647
18. Torabmostaedi H, Zhang T, Foot P, Dembele S, Fernandez C (2013) Process control for the synthesis of $ZrO_2$ nanoparticles using FSP at high production rate. Powder Technol 246:419–433
19. Khan S, Kim J, Sotto A, der Bruggen BV (2015) Humic acid fouling in a submerged photocatalytic membrane reactor with binary $TiO_2$–$ZrO_2$ particles. J Ind Eng Chem 21:779–786
20. Smirnova N, Gnatyuk Y, Eremenko A, Kolbasov G, Vorobetz V, Kolbasova I, Linyucheva O (2006) Photoelectrochemical characterization and photocatalytic properties of mesoporous $TiO_2$/$ZrO_2$ films. Int J Photoenergy 2006:1–6
21. Wu B, Yuan R, Fu X (2009) Structural characterization and photocatalytic activity of hollow binary $ZrO_2$/$TiO_2$ oxide fibers. J Solid State Chem 182:560–565
22. Kambur A, Pozan GS, Boz I (2012) Preparation, characterization and photocatalytic activity of $TiO_2$-$ZrO_2$ binary oxide nanoparticles. Appl Catal B Environ 115–116:149–158
23. Duan N, Lin H, Li L, Hu J, Bi L, Lu H, Weng X, Xie J, Deng L (2013) $ZrO_2$–$TiO_2$ thin films: a new material system for mid-infrared integrated photonics. Opt Mater Express 3(9):1537–1545
24. Tomar LJ, Bhatt PJ, Desai RK, Chakrabarty BS (2014) Effect of preparation method on optical and structural properties of $TiO_2$/$ZrO_2$ nanocomposite. J Nano Adv Mater 2(1):27–33
25. Pirzada BM, Mir NA, Qutub N, Mehraj O, Sabir S, Muneer M (2015) Synthesis, characterization and optimization of photocatalytic activity of $TiO_2$/$ZrO_2$ nanocomposite heterostructures. Mater Sci Eng B 193:137–145
26. Vaizoğullar AI, Balci A, Uğurlu M, Karaoğlu MH (2016) Synthesis of TiO2 and ZrO2/TiO2 composite microspheres and their photo-catalytic degradation of methylene blue. AKU J Sci Eng 16(011203):54–60
27. Moriya I (2018) Reduction of $CO_2$ over the $TiO_2$/$ZrO_2$ composites covered with a very thin layer of water under solar irradiation. Adv Mater Sci 3(1):1–2
28. Mote VD, Purushotham Y, Dole BN (2012) Williamson–Hall analysis in estimation of lattice strain in nanometer-sized ZnO particles. J Theor Appl Phys 6:6
29. Köferstein R, Jäger L, Ebbinghaus SG (2013) Magnetic and optical investigations on $LaFeO_3$ powders with different particle sizes and corresponding ceramics. Solid State Ionics 249–250:1–5
30. Lopez R, Gomez R (2012) Band-gap energy estimation from diffuse reflectance measurements on sol–gel and commercial $TiO_2$: a comparative study. J Sol Gel Sci Technol 61:1–7
31. Li M, Li X, Jiang G, He G (2015) Hierarchically macro-mesoporous $ZrO_2$–$TiO_2$ composites with enhanced photocatalytic activity. Ceram Int 41:5749–5757
32. Raj KJA, Viswanathan B (2009) Effect of surface area, pore volume and particle size of P25 titania on the phase transformation of anatase to rutile. Indian J Chem 48A:1378–1382

33. Wang Z, Cai W, Hong X, Zhao X, Xu F, Cai C (2005) Photocatalytic degradation of phenol in aqueous nitrogen-doped $TiO_2$ suspensions with various light sources. Appl Catal B 57:223–231
34. Fan X, Chen X, Zhu S, Li Z, Yu T, Ye J, Zou Z (2008) The structural, physical and photocatalytic properties of the mesoporous Cr-doped $TiO_2$. J Mol Catal A Chem 284:155–160
35. Wang S, Li D, Sun C, Yang S, Guan Y, He H (2014) Synthesis and characterization of g-$C_3N_4$/$Ag_3VO_4$ composites with significantly enhanced visible-light photocatalytic activity for triphenylmethane dye degradation. Appl Catal B Environ 144:885–892
36. Li K, An X, Park KH, Khraisheh M, Tang J (2014) A critical review of $CO_2$ photoconversion: catalysts and reactors. Catal Today 224:3–12
37. Chung WH, Lu CS, Lin WY, Wang JX, Wu CW, Chen CC (2012) Determining the degradation efficiency and mechanisms of ethyl violet using HPLC–PDA–ESI–MS and GC–MS. Chem Cent J 6:63
38. Rosman N, Salleh WNW, Ismail AF, Jaafar J, Harun Z, Aziz F, Mohamed MA, Ohtani B, Takashima M (2018) Photocatalytic degradation of phenol over visible light active ZnO/$Ag_2CO_3$/$Ag_2O$ nanocomposites heterojunction. J Photochem Photobiol A 364:602–612
39. Elbasuney S, Elsayed MA, Mostafa SF, Khalil WF (2019) $MnO_2$ nanoparticles supported on porous $Al_2O_3$ substrate for wastewater treatment: synergy of adsorption, oxidation, and photocatalysis. J Inorg Organomet Polym Mater. https://doi.org/10.1007/s10904-018-01057-0
40. Wu C, Zhao X, Ren Y, Yue Y, Hua W, Cao Y, Tang Y, Gao Z (2005) Gas-phase photo-oxidations of organic compounds over different forms of zirconia. J Mol Catal A Chem 229:233–239